ADVANCED MATERIALS
www.advmat.de

Tunable Phonon Polariton Hybridization in a Van der Waals Hetero-Bicrystal

Lukas Wehmeier, Shang-Jie Yu, Xinzhong Chen, Rafael A. Mayer, Langlang Xiong, Helen Yao, Yue Jiang, Jenny Hu, Eli Janzen, James H. Edgar, Xiaolin Zheng, Tony F. Heinz, D. N. Basov, Christopher C. Homes, Guangwei Hu, G. Lawrence Carr, Mengkun Liu,* and Jonathan A. Fan**

Phonon polaritons, the hybrid quasiparticles resulting from the coupling of photons and lattice vibrations, have gained significant attention in the field of layered van der Waals heterostructures. Particular interest has been paid to hetero-bicrystals composed of molybdenum oxide (MoO_3) and hexagonal boron nitride (hBN), which feature polariton dispersion tailorable via avoided polariton mode crossings. In this work, the polariton eigenmodes in MoO_3-hBN hetero-bicrystals self-assembled on ultrasmooth gold are systematically studied using synchrotron infrared nanospectroscopy. It is experimentally demonstrated that the spectral gap in bicrystal dispersion and corresponding regimes of negative refraction can be tuned by material layer thickness, and these results are quantitatively matched with a simple analytic model. Polaritonic cavity modes and polariton propagation along "forbidden" directions are also investigated in microscale bicrystals, which arise from the finite in-plane dimension of the synthesized MoO_3 micro-ribbons. The findings shed light on the unique dispersion properties of polaritons in van der Waals heterostructures and pave the way for applications leveraging deeply sub-wavelength mid-infrared light-matter interactions.

1. Introduction

Van der Waals materials have emerged as a versatile platform for hosting polaritons,[1,2] which are hybrid light-matter quasiparticles that enable light confinement and control at the nanoscale.[1–3] This versatility arises in part because these materials feature exceptional intrinsic properties, including ultralow losses, high quality factors, and long polariton lifetimes. Along these lines, hexagonal boron nitride (hBN)[4–15] and alpha phase molybdenum trioxide (MoO_3)[14–26] have been shown to exhibit best-in-class polaritonic properties and have become two of the most studied polaritonic materials in the recent literature. This versatility also arises because van der Waals materials can be readily stacked to produce heterostructures with designed optical properties.[27] For the

L. Wehmeier, C. C. Homes, G. L. Carr, M. Liu
National Synchrotron Light Source II
Brookhaven National Laboratory
Upton, NY 11973, USA
E-mail: lwehmeier@bnl.gov; mengkun.liu@stonybrook.edu

L. Wehmeier, X. Chen, R. A. Mayer, M. Liu
Department of Physics and Astronomy
Stony Brook University
Stony Brook, NY 11794, USA

S.-J. Yu, J. A. Fan
Department of Electrical Engineering
Stanford University
Stanford, CA 94305, USA
E-mail: jonfan@stanford.edu

The ORCID identification number(s) for the author(s) of this article can be found under https://doi.org/10.1002/adma.202401349

DOI: 10.1002/adma.202401349

X. Chen, D. N. Basov
Department of Physics
Columbia University
New York, NY 10027, USA

L. Xiong, G. Hu
Nanyang Technological University
School of Electrical and Electronic Engineering
Singapore 637371

H. Yao
Department of Materials Science and Engineering
Stanford University
Stanford CA 94305, USA

H. Yao, J. Hu, T. F. Heinz
SLAC National Accelerator Laboratory
Menlo Park, CA 94025, USA

Y. Jiang, X. Zheng
Department of Mechanical Engineering
Stanford University
Stanford, CA 94305, USA

J. Hu, T. F. Heinz
Department of Applied Physics
Stanford University
Stanford, CA 94305, USA

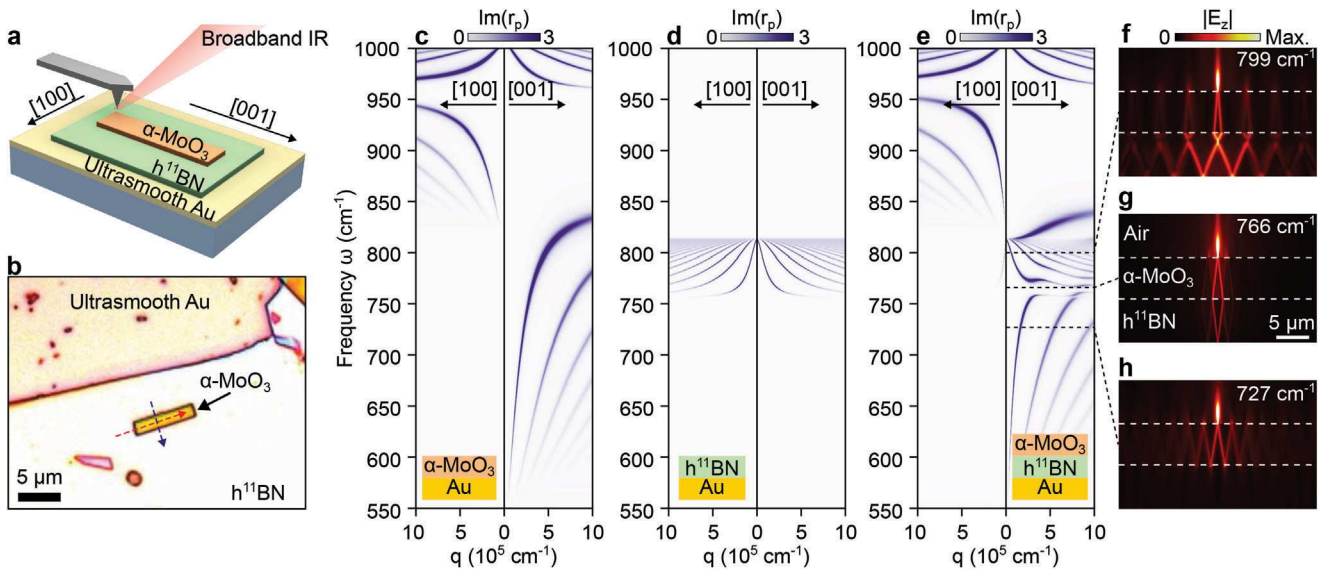

Figure 1. Polariton dispersion of an hBN-MoO_3 hetero-bicrystal. a) Synchrotron-based infrared near-field nanospectroscopy is employed to study hetero-bicrystals comprising MoO_3 microribbons on exfoliated, isotopically pure hBN flakes on an ultrasmooth gold substrate. b) Optical microscopy image of a representative hetero-bicrystal. Colored illumination and thin-film interference induce a thickness-dependent optical contrast. c–e) Calculated imaginary parts of the Fresnel reflection coefficient Im(r_p), which illustrates the dispersion of the polariton mode, for slabs of c) MoO_3, d) hBN, and e) a MoO_3-hBN hetero-bicrystal. The MoO_3 and hBN slabs in each calculation are 100 nm thick. f–h) Numerical simulations of electric field strength in the cross-section of an MoO_3-hBN bicrystal with slab thicknesses of 1 μm, at frequencies f) 799 cm^{-1}, g) 766 cm^{-1}, and h) 727 cm^{-1}. The field profile in (g) represents the bicrystal regime that supports a negative refraction cavity mode. The scale bar applies only to the horizontal direction.

examples of hBN and MoO_3, stacking and twisting two flakes of the same material can produce a plethora of new properties and options for polaritonic tuning.[17,18,28,29]

Single hetero-bicrystals comprising combinations of hBN and MoO_3 are a particularly rich system for the study of new polaritonic behavior. In an initial investigation, hBN-MoO_3 hetero-bicrystals were found to showcase optical phenomena such as negative polaritonic refraction, closed-loop light trajectories, polaritonic level repulsion, and avoided mode crossings.[15] One of the most striking features is the emergence of a new spectral gap in the polariton dispersion, which results from polaritonic level repulsion and strong mode coupling. However, systematic experimental studies of these heterostructures have proven to be elusive, calling for more efforts on the preparation of high-quality large-area samples and their broadband nanospectroscopic investigation, as well as the simplified but insightful physical interpretations.

In this report, we experimentally explore the evolution of polariton dispersion as a function of heterostructure geometry through the systematic fabrication and optical study of hetero-bicrystals comprising isotopically pure hBN and MoO_3 layers on an ultrasmooth gold substrate (**Figure 1**a,b). Our study leverages crystalline MoO_3 microstructures[22,26] that are chemically grown with high yield and a distribution of thicknesses, thereby facilitating the assembly of ensembles of high quality hetero-bicrystals. Isotopically pure hBN crystals[10–12] are used because they feature exceptionally low loss and polaritonic modes that ideally overlap with those in MoO_3. Experimental analysis is performed using synchrotron infrared nanospectroscopy (SINS), which utilizes the scattering of infrared radiation off an atomic force microscopy (AFM) tip to perform polariton interferometry[15–26,30–38] and enables direct visualization of polariton mode dispersion. We observe with SINS that the spectral position and width of the spectral gap in the polariton dispersion can be tuned via the thickness ratio of its constituting hBN and MoO_3 crystals, and these trends quantitatively match with analytic models. We further demonstrate that with our unique sample configuration, optical signatures of negative refraction cavity modes can be directly read out in the SINS hyperspectral line scans. We additionally explore the effects that are associated with the finite in-plane dimension of microscale bicrystals, such as the existence of polaritonic cavity modes and polaritonic propagation along "forbidden" directions.

2. Results

To understand and interpret the polaritonic dispersive response of an hBN-MoO_3 bicrystal on ultrasmooth gold, it is instructive to first examine the dispersion curves of the individual constituent materials and the bicrystal on gold. At mid-infrared wavelengths, the gold effectively functions as a perfect electrical conductor (PEC) and supports ideal image polaritons.[39] The polaritonic responses of van der Waals films on gold therefore follow those of the antisymmetric modes within van der Waals films with double the thickness and clad in air. Branches in polaritonic dispersion

E. Janzen, J. H. Edgar
Tim Taylor Department of Chemical Engineering, Durland Hall
Kansas State University
Manhattan, KS 66506, USA

can be realized by calculating the maxima of the imaginary part of the p-polarized Fresnel reflection coefficient, $\mathrm{Im}(r_p)$.[5,30]

Figure 1c shows $\mathrm{Im}(r_p)$ for a 100 nm-thick MoO_3 flake for a broad range of incident frequencies ω and in-plane momenta q. The in-plane anisotropy[16] of MoO_3 is clear as the polariton branches differ significantly for q along the crystalline [100] direction (left in Figure 1c) versus the [001] direction (right in Figure 1c). Unlike MoO_3, hBN supports in-plane isotropic polariton propagation and shows a single hyperbolic reststrahlen band[7] from around 760 to 820 cm^{-1}, as illustrated for a 100 nm-thick hBN flake in Figure 1d. Notably, hBN supports negative dispersion (decreasing q with increasing frequency ω) while MoO_3 supports positive dispersion (increasing q with increasing ω) in this spectral range.

The combination of materials with positive and negative dispersion in the same spectral range, which is the case for the hBN-MoO_3 bicrystal,[15] is a key ingredient to realizing new polaritonic behavior. Figure 1e shows $\mathrm{Im}(r_p)$ for a 200 nm-thick bicrystal consisting of a 100 nm-thick MoO_3 slab on a 100 nm-thick hBN slab on the gold substrate. Within the spectral range where the polariton branches of hBN and MoO_3 overlap, we observe the hybridization of the hyperbolic phonon polaritons of both materials, that is, the formation of a new coupled polariton mode that is intrinsic to the hBN-MoO_3 heterostructure.[15] Notably, the hybridized polaritons show spectral regions with positive and negative dispersion separated by a spectral gap where no polariton propagation is allowed in the bicrystal. For this case where hBN and MoO_3 have the same thickness, the center of the gap (ω_0) is at 766 cm^{-1}.

We further elucidate the underlying light-matter interactions near and in the polaritonic spectral gap by performing 2D full-wave simulations of an electric dipole excitation located above the bicrystal. This excitation condition follows our experimental configuration and is consistent with nanoscopic tip illumination in SINS. We consider 1 µm-thick van der Waals slabs in this analysis because polaritonic propagation follows ray-like behavior in such thick slabs and is more straightforward to interpret (see Experimental Section, Figures S3 and S4, Supporting Information). Figure 1f–h shows the electric field produced by the dipole within a cross-section of the bicrystal at frequencies of 727, 766, and 799 cm^{-1}, respectively. At ω = 727 cm^{-1}, the excitation frequency is outside the hBN reststrahlen band, and the polaritonic behavior is dominated by the MoO_3 response, with ray-like polariton propagation through the MoO_3 crystal. At ω = 799 cm^{-1}, the roles of hBN and MoO_3 are interchanged, and polaritonic dispersion, specifically the lateral displacement of the polaritonic rays, is dominated by propagation through the hBN crystal. The most intriguing behavior is observed at ω = 766 cm^{-1}, which corresponds to ω_0. There is a diamond-shaped closed-loop trajectory of the polaritons (Figure 1g), resulting from negative refraction of the polaritons at the hBN-MoO_3 interface.[15] Importantly, these simulations indicate that the negative refraction cavity mode within the bicrystal can be directly excited by and read out with the nanoscopic tip in SINS.

For our experimental efforts, sample preparation is performed by transferring microscale MoO_3 crystals onto hBN flakes,[10–12] which are initially exfoliated onto ultrasmooth gold. The MoO_3 crystals are grown using flame vapor deposition (FVD), from which densely packed microscale ribbons with a wide range of thicknesses are produced in a single batch.[22] These materials have been previously characterized to support polaritonic lifetimes matching those from single crystal exfoliated samples, and they have atomically sharp edge interfaces that are ideal for polariton interferometry. The isotopically pure $h^{11}BN$ flakes are relatively large, with dimensions on the order of 100 µm x 100 µm, such that multiple hetero-bicrystal structures can be readily formed by transferring multiple MoO_3 crystals onto a single $h^{11}BN$ flake. Our utilization of a gold substrate with atomic smoothness, prepared using template stripping, ensures that the interface between hBN and the substrate is ideal and that optical losses due to surface roughness are minimized.

SINS analyses[8,22,34–37,40] of two representative hetero-bicrystals are presented in **Figure 2**. Experimental details and data for two additional bicrystals are in the Experimental Section. AFM images of the bicrystal topographies (Figure 2a,d) show MoO_3 crystals with approximately rectangular shapes, homogeneous thicknesses, and clean crystal edges. The long axes of the MoO_3 crystals are aligned with their crystalline [001] direction, which is consistent with previous MoO_3 microribbon studies[22] and is confirmed by the nanospectroscopy analysis performed here. As the [001] direction of MoO_3 corresponds to the direction featuring the hBN-MoO_3 bicrystal polaritonic gap[15] (Figure 1e), we first perform hyperspectral line scans along this direction for both bicrystals (Figure 2a,d, arrow). The resulting hyperspectral data (Figure 2b,e) at ω < 820 cm^{-1} show clear fringe patterns. As these stem from the interference of hybridized bicrystal polaritons launched by the tip and reflected back from the MoO_3 crystal edges, this is referred to as polariton interferometry.[15–26,30–38] The observation of clearly discernable fringes with high signal-to-noise across the mid-infrared band can be attributed to the high degree of crystalline sample quality, the high intensity of the light source, and the MoO_3-on-hBN ordering of the bicrystal. As discussed in the Experimental Section, the placement of MoO_3 on hBN results in a more uniform spectral distribution of the bicrystal's polaritonic features compared to heterostructures comprising an inverted layer order.

Polariton dispersion can be directly extracted by quantifying fringe spacing variation as a function of frequency, as the fringe spacing corresponds to half the polariton wavelength. Experimental values for polariton dispersion are extracted by fitting a decaying sine wave of the form exp(ikx). The resulting Re(k) is represented by yellow dots in Figure 2c,f, together with dispersion curves calculated from $\mathrm{Im}(r_p)$. The experimental data and calculations quantitatively agree and show that the polariton momentum increases when approaching ω_0 from both higher and lower frequencies for both samples. The reduced number of observable polariton fringes in Figure 2b,e indicates that the polariton quality factor, $Q(\omega)$, decreases as the frequency approaches the polaritonic gap.

Notably, we observe a pronounced SINS intensity peak in the hyperspectral scan of each bicrystal (Figure 2b,e, red arrow) in the spectral range around the polaritonic bandgap, which directly corresponds to the calculated ω_0's in Figure 2c,f (dashed line) and indicates that the polaritonic bandgap is tunable based on bicrystal geometry. The origins of these peaks can be understood by interpreting an individual bicrystal as a superlens[7,9,41–45] that utilizes the negative refraction cavity mode to image a dipole source at the bicrystal's top surface (i.e., the physical MoO_3-air interface) to

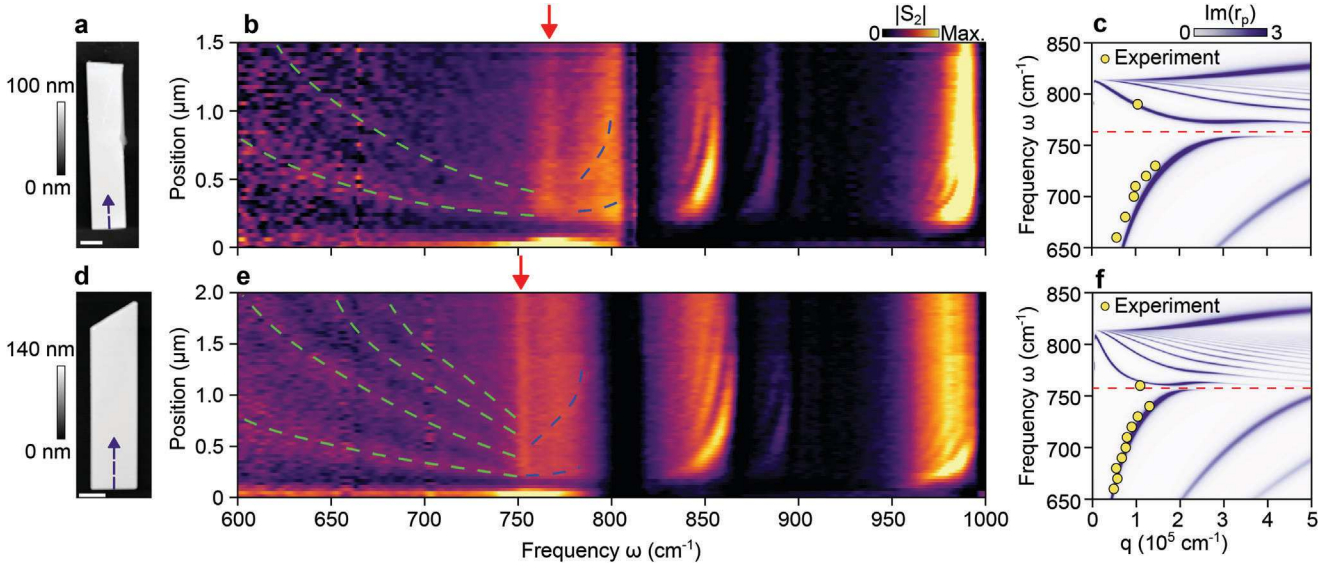

Figure 2. SINS hyperspectral line scans of hetero-bicrystals along the MoO_3 [001] direction. a) Atomic force microscopy image of the topography of an 88 nm-thick MoO_3 microribbon on top of an 83 nm-thick hBN flake. Scale bar: 1 μm. b) Hyperspectral line scan acquired by taking infrared near-field point nanospectra along the purple arrow marked in (a). Fringe patterns are attributed to the interference of hyperbolic phonon polaritons. The gap frequency, ω_0, manifests as a bright vertical line marked by a red arrow. c) Calculated dispersion curves for the bicrystal in (a) together with experimental dispersion values extracted from (b) (yellow dots, error bars smaller than symbol size). d–f) Same data as in (a–c) for a bicrystal consisting of a 116 nm-thick MoO_3 microribbon and a 242 nm-thick hBN flake.

its image plane at the bicrystal's bottom surface (i.e., the physical hBN-Au interface) with subwavelength resolution. The gold, serving as an ideal reflector in the PEC limit, reflects this radiation back through the superlens, which refocuses at the dipole source location. In this manner, the SINS AFM tip naturally serves as both the dipole source and detector for sensing the strong field intensities from the refocused radiation at ω_0. This double role of the tip is special to the case of a PEC substrate. We can generalize the superlens interpretation to arbitrary substrates, stating that at ω_0 we are effectively probing the substrate underneath the bicrystal. For example, using SiO_2 substrate results in a reduced near-field amplitude close to ω_0,[15] while here we observe an increased near-field response around ω_0 in Figure 2c,f due to the comparably large near-field response of gold.

The hyperspectral line scans also reveal polaritonic modes at frequencies outside of the hybridized bicrystal polariton frequency range. Fringes at $\omega > 950$ cm^{-1} can be directly assigned to in-plane MoO_3 hyperbolic phonon polariton modes that are fully decoupled from the hBN reststrahlen band (Figure 1c,e).[16] Interestingly, we observe polaritonic fringes in the intermediate spectral range 820 cm^{-1} $< \omega <$ 950 cm^{-1}, which cannot be assigned to polaritonic modes that naturally propagate along the [001] direction of MoO_3 or hBN. In fact, polaritonic modes in these materials only exist along the [100] direction in infinite in-plane MoO_3 (Figure 1c,d). We attribute these modes to geometric confinement effects in our microribbon system, which have been recently studied in MoO_3 cavities[25] and can allow [001] waveguide modes to propagate along the [100] direction. Further numerical analysis of this phenomenon in our bicrystal system is provided later in this study.

SINS hyperspectral line scans along the [100] direction of the bicrystals reveal strong polaritonic Fabry-Pérot cavity modes that are enabled by the microscale width of the MoO_3 ribbons (**Figure 3**). Along this crystal direction, the polaritonic contributions from hBN and MoO_3 are in distinct spectral bands and do not hybridize. In the spectral range $\omega > 820$ cm^{-1}, MoO_3 supports polaritonic modes while hBN effectively functions as a passive dielectric substrate. The fringe patterns in Figure 3b,e can therefore be interpreted as MoO_3 polaritonic Fabry-Pérot cavity modes[19,21–23,25,26,36,38,46,47] that are constrained to the finite-sized MoO_3 crystal. The overall polaritonic dispersion is well described via the calculated Im(r_p) in Figure 3c,f. However, as the analytical calculation of Im(r_p) implicitly assumes infinite in-plane sample dimensions, it does not explain the observed cavity modes. The latter are included in numerical simulations that we present later. In the spectral range 750 cm^{-1} $< \omega <$ 820 cm^{-1}, hBN supports polaritonic modes while MoO_3 effectively functions as a passive dielectric. The fringes are attributed to hBN polariton Fabry-Pérot cavity modes in which the MoO_3 microribbon serves as an external Fabry-Pérot cavity that facilitates hBN polariton reflection[48] at the MoO_3 crystal edge.

The dispersion properties and tunability of the polariton gap for hybridized bicrystal polaritons along the MoO_3 [001] direction can be further analyzed with analytic modeling. We summarize here the key results and provide a detailed discussion of our approach in the Experimental Section. The dispersion relations can be extracted from the following transcendental expression:

$$q(\omega) = \frac{\psi_{MoO_3}}{d_{MoO_3}}\left[\operatorname{atan}\left(-\frac{\epsilon_{M,oop}}{\psi_{MoO_3}}\frac{1}{\epsilon_1}\right) + \operatorname{atan}\left(-\frac{\epsilon_{M,oop}}{\psi_{MoO_3}}\frac{\psi_{hBN}\tan\left(\frac{qd_{hBN}}{\psi_{hBN}}\right)}{\epsilon_{h,oop}}\right) + l\pi\right], \quad l = 0, 1, 2 \qquad (1)$$

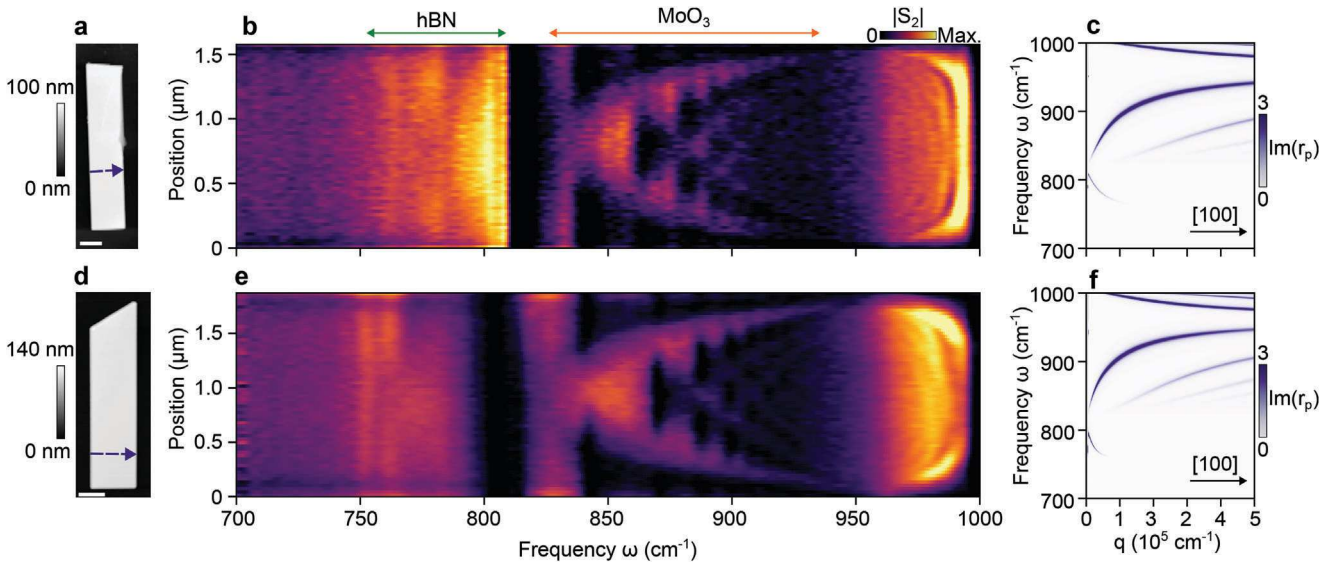

Figure 3. hBN-MoO_3 bicrystal cavity modes along the MoO_3 [100] direction. a) Atomic force microscopy image of the same bicrystal shown in Figure 2a, together with a purple arrow denoting the SINS scan along the [100] direction of MoO_3. Scale bar: 1 μm. b) Hyperspectral line scan of the bicrystal in (a), which reveals hyperbolic phonon polariton cavity modes from the MoO_3 and hBN slabs. c) Calculated $Im(r_p)$ for the MoO_3-hBN bicrystal in (a). d–f) Same data as in (a–c) for the bicrystal featured in Figure 2d.

q is the in-plane wavevector, ϵ_1, $\epsilon_{M,i}$, and $\epsilon_{h,i}$ represent the background permittivity, MoO_3 permittivity, and hBN permittivity, respectively ($i \in ip$, oop, where the oop denotes the out-of-plane direction and ip denotes the in-plane direction), d_{MoO_3} and d_{hBN} refer to the respective thicknesses of the MoO_3 and hBN crystals, $\psi_{MoO_3} = \sqrt{-\frac{\epsilon_{M,oop}}{\epsilon_{M,\ ip}}}$, and $\psi_{hBN} = \sqrt{-\frac{\epsilon_{h,oop}}{\epsilon_{h,\ ip}}}$. The dispersion relations are computed by sweeping through l and real frequency to solve for q. Introducing material loss with the use of complex valued permittivities transforms q into a complex number and enables calculation of the polariton quality factor $Q(\omega) = \frac{Re(q)}{Im(q)}$.

In the approximation where polariton propagation is treated in the ray limit,[9,15] the expression for gap frequency ω_0 can be simplified to:

$$\frac{\tan\theta_{MoO_3}(\omega_0)}{\tan\theta_{hBN}(\omega_0)} = \frac{d_{hBN}}{d_{MoO_3}} \quad (2)$$

$\theta_{hBN}(\omega)$ and $\theta_{MoO_3}(\omega)$ refer to the polariton propagation angle with respect to the surface normal in each material. The dependence of θ on the frequency ω is provided by the anisotropic permittivity tensor of each material.[9] For a more rigorous treatment, ω_0 also can be determined through the utilization of Equation (1) in the following way. First, the dispersion of the individual MoO_3 and hBN slabs can be solved by setting d_{MoO_3} or $d_{hBN} = 0$ in Equation (1). Second, the strongest coupling frequency, that is, the gap frequency ω_0, can be identified by examining the resonance frequencies of these slabs at a fixed momentum.[49]

We see from this analysis that the key parameter for ω_0 tuning is the d_{MoO3}/d_{hBN} thickness ratio. To support this observation, we calculate and plot the dispersion relations for different bicrystals consisting of 100 nm-thick MoO_3 and hBN with thicknesses ranging from 20 nm ($\frac{d_{hBN}}{d_{MoO_3}} = 0.2$) to 250 nm ($\frac{d_{hBN}}{d_{MoO_3}} = 2.5$) (**Figure** 4a–d). Dispersion curves calculated using $Im(r_p)$ (blue lines) and Equation (1) (green dots) match, indicating the consistency of these computational methods. The plots clearly indicate that ω_0, delineated by the red dashed lines in the plots, tunes from 815 to 765 cm^{-1} as the thickness ratio varies. These theoretical trends match well with experimental values for ω_0 (Figure 4e), which are extracted from the SINS intensity peaks in the hyperspectral scans of four different bicrystals (the two samples in Figure 2 and the two samples in Figures S8 and S9, Supporting Information). The theoretical trends in quality factor (i.e., $Q(\omega)$ reduction for frequencies near the bandgap) also are consistent with experiment and reinforce the idea that polaritonic behavior in our bicrystals is well described by our analytic models.

The dispersion curves also provide a quantitative assessment of the gap width, $\Delta\omega$, which is an important parameter for characterizing polaritonic coupling. A rigorous definition of the gap width is provided in the Experimental Section. Figure 4f shows $\Delta\omega$ as a function of $\frac{d_{hBN}}{d_{MoO_3}}$, from which we find a maximum gap width when the thickness ratio is around 0.3. The presence of an ideal thickness ratio for polaritonic coupling can be intuitively understood in the context of polariton momentum matching in both materials. For MoO_3 and hBN of the same thickness, polaritons are not momentum matched, as the MoO_3 polariton momentum is about a factor of three higher than that of hBN (Figure 1c,d). However, due to the approximate inverse scaling of hyperbolic phonon polariton momentum with material thickness,[4,7,9] polariton momenta in both materials are matched when the MoO_3 crystal is ≈3× thicker than the hBN crystal. Qualitatively, momentum-matched polaritons interact more strongly with each other, thereby introducing a larger gap width. Quantitatively, momentum-matched polaritons yield mode overlap integrals with maximal values in expressions for mode coupling.

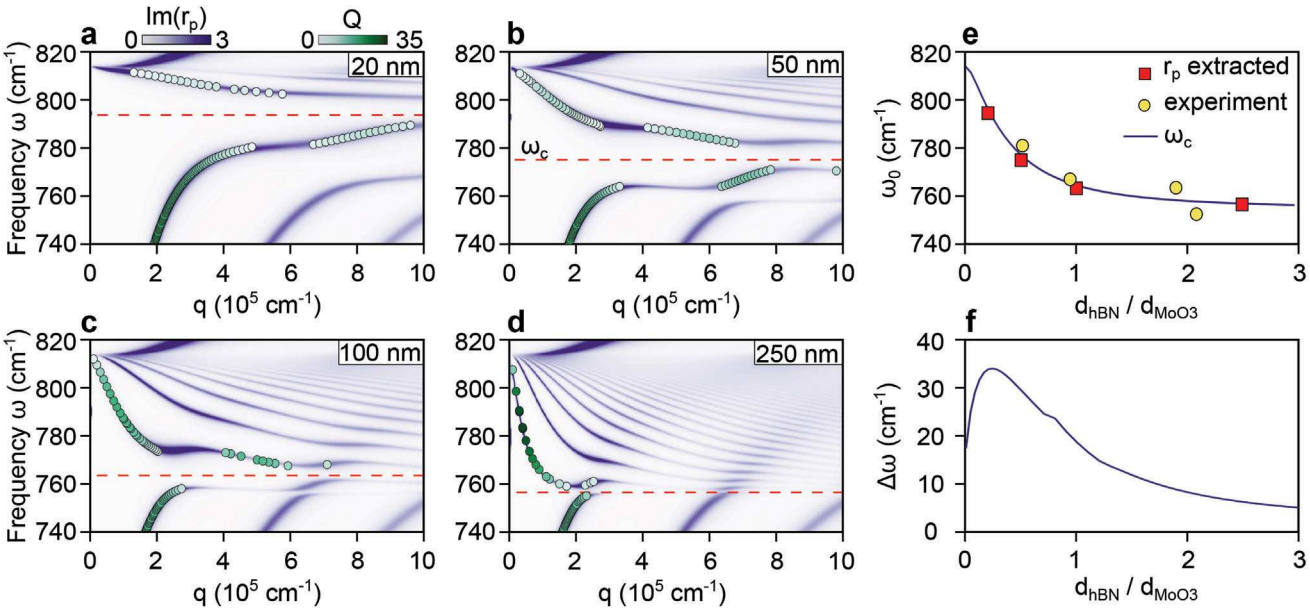

Figure 4. Negative refraction and spectral gap tuning of bicrystals along the MoO_3 [001] direction by changing the hBN-MoO_3 thickness ratio. a–d) Calculated Im(r_p) for bicrystals consisting of a 100 nm-thick MoO_3 slab and hBN slabs with thicknesses of a) 20, b) 50, c) 100, and d) 250 nm. The shades of green dots represent the quality factor of the fundamental polariton branch calculated from analytic dispersion relations. The red dashed lines mark the spectral polaritonic gap positions. Im(r_p) calculations for additional thickness values are shown in Figure S5, Supporting Information. e) Dependence of the polaritonic gap frequency on hBN-MoO_3 thickness ratio. The line shows the theoretical trend from Equation (2), the red squares are calculated values from the Im(r_p)-maps in (a–d), and the yellow dots are experimental values from the hyperspectral line scans of four different samples. f) Calculated dependence of the gap width $\Delta\omega$ on the hBN-MoO_3 thickness ratio.

In the final part of our analysis, we perform full 3D full-wave modeling of a finite-sized bicrystal, which we use to rigorously capture all observed polaritonic behavior in our SINS experiments. We employ 3D full-wave finite-difference time-domain (3D FDTD) simulations using the fast numerical solver Tidy3D, and we capture the SINS experimental flow by scanning a broadband dipole excitation source across the bicrystal. The simulated bicrystal consists of a rectangular 1.5 µm-wide, 8.0 µm-long MoO_3 microribbon on a larger hBN crystal on a gold substrate, which is close to the experimental bicrystal geometry featured in Figure 2a. The dipole source is located 200 nm above the MoO_3 crystal and we monitor the out-of-plane component of the electric field 40 nm above the crystal. The hyperspectral line scans are taken along the reflection symmetry planes of the bicrystal along the MoO_3 [001] and [100] directions and are shown in **Figure 5**a,b, respectively. Overall, there is excellent agreement between our numerical and experimental line scans, including the presence of hybridized bicrystal polaritons at $\omega < 820$ cm^{-1}, enhanced near-field intensity at the polaritonic bandgap at $\omega_0 = 766$ cm^{-1} (further supporting our interpretation of the bicrystal as a superlens at ω_0), and forbidden guided modes at 750 cm$^{-1} \lesssim \omega \lesssim 820$ cm^{-1} along the [001] direction. We also observe clear signatures of MoO_3 and hBN Fabry-Pérot cavity modes along the [100] direction. The plots additionally show that "allowed" polariton modes along [100] support positive dispersion while the dispersion is inverted for the forbidden polariton modes along the [001] direction, which agrees with the experiments and further confirms the ability of these simulations to capture subtle polaritonic behavior.

To visualize polaritonic propagation more directly in our finite-sized bicrystals, we utilize 3D FDTD simulations to produce electric field profiles for dipole excitations with a fixed position and varying frequency. False color field plots of the real part of the electric field along the out-of-plane direction, Re(E_z), are summarized in Figure 5c. We observe the characteristic wavefronts associated with MoO_3 hyperbolic polaritons,[16,20,21,24] that is, in-plane elliptical wavefronts around 1000 cm^{-1} and in-plane hyperbolic concave wavefronts around 600 cm^{-1}. In spectral regions where the MoO_3 dimensions are small compared to the polariton decay length (e.g., around 860 cm^{-1}), there are more complex standing wave patterns that are formed not only along the direction where hyperbolic polariton propagation is allowed (e.g., [100] direction at 860 cm^{-1}, refer to Figure 1e), but also along the orthogonal direction where propagation is forbidden (e.g., [001] direction at 860 cm^{-1}). These standing wave patterns illustrate how geometrical confinement can enable polariton propagation in the forbidden direction.[19,25]

3. Conclusion

In summary, we have performed a systematic theoretical and experimental analysis of the polaritonic properties of finite-sized hBN-MoO_3 hetero-bicrystals. We demonstrate that the thickness ratio of the van der Waals heterostructure can be used to explicitly tune the polaritonic gap position and width, and we experimentally measure signatures of the negative refraction cavity mode within the polaritonic bandgap that tunes with thickness ratio. Compared to alternative schemes for negative refraction in van der Waals materials based on graphene plasmon polaritons,[24]

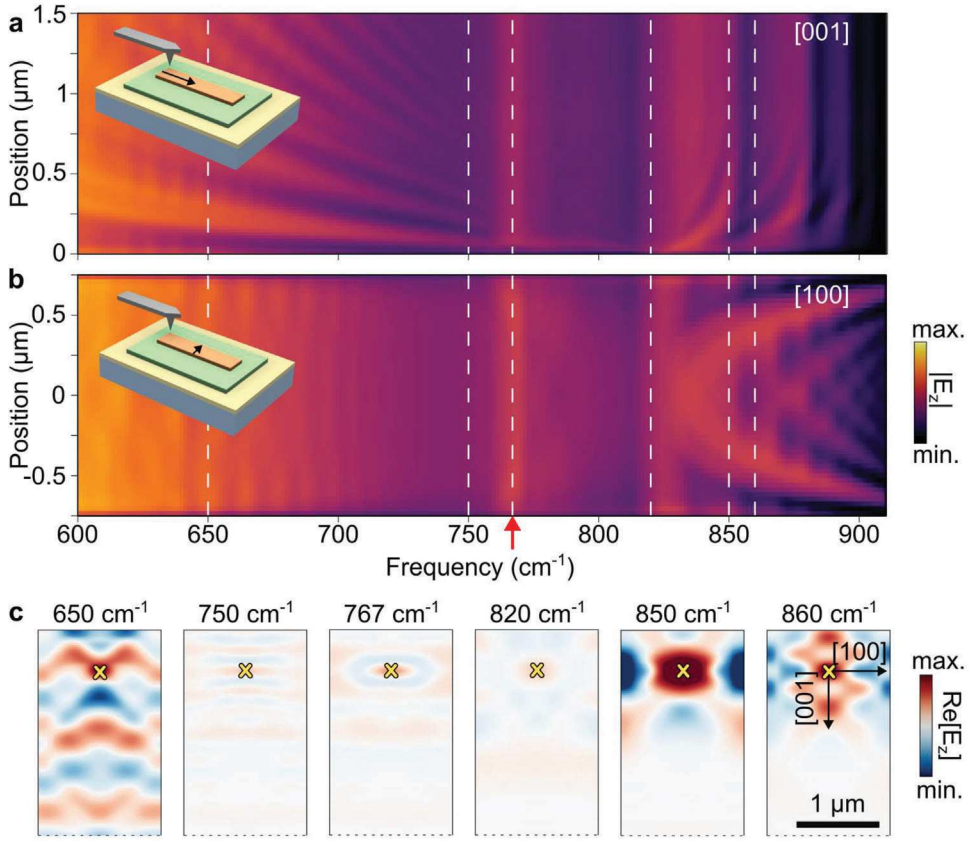

Figure 5. 3D numerical simulations of a finite-sized bicrystal. a,b) Simulated hyperspectral line scan along the a) [001] and b) [100] direction of a finite-sized MoO_3 microribbon on hBN on gold. The bicrystal consists of a 100 nm-thick MoO_3 microribbon and a 100 nm-thick hBN flake. Matching the experimental results in Figure 2, the gap frequency, ω_0, manifests as a bright vertical line marked by a red arrow. Dashed white lines in (a,b) mark the spectral positions of the simulations shown in (c). Insets: top view schematic of the simulated bicrystal and line scan positions. c) Numerical simulations of the out-of-plane component of the electric field at the surface of the bicrystal, given vertical dipolar excitations at the points marked by x's, for different frequencies.

our work does not rely on doping-dependent plasmonic phenomena but employs only low-loss phonon polariton modes. We also characterize forbidden polaritonic modes[25] and polaritonic Fabry-Pérot cavity modes[19,21–23,25,26,36,38,46,47] that arise from finite-size effects of our bicrystal system. All of our experimental findings are corroborated by a combination of analytic and full 3D numerical calculations, which capture real-space phenomena that are not covered via simpler analyses such as the calculation of $\mathrm{Im}(r_p)$. Future research directions include the explicit characterization of the bicrystal as a tunable superlens and the development of new flame vapor-deposited van der Waals recipes, which can enable the high throughput assembly and characterization of new classes of hetero-bicrystals.

4. Experimental Section

Sample Preparation: hBN-MoO_3 bicrystals consisting of a smaller MoO_3 flake on top of a larger (≈100 μm x 100 μm), isotopically pure $h^{11}BN$ crystal were studied. The bicrystal was placed on top of an ultrasmooth gold (Au) substrate.

Growth of MoO_3: The synthesis of α-MoO_3 micro- and nanostructures was based on the previously reported FVD method. The flame synthesis setup in this work has a 6 cm diameter premixed flat-flame burner (McKenna burner, Holthuis & Associates) with CH_4 as the fuel and air as the oxidizer. The fuel-to-air equivalence ratio of the flame was fixed as 0.88 with a CH_4 flow rate of 1.80 standard liter per minute (SLPM) and an airflow rate of 19.48 SLPM. The equivalence ratio was defined as the ratio of actual fuel/oxidizer molar ratio to the stoichiometric fuel/oxidizer molar ratio. A 4 cm × 4 cm Mo mesh prepared from Mo wires (0.203 mm in diameter, 99.9%, Alfa Aesar) was placed over the premixed flame as the solid Mo source. The area density of this Mo source was about 18 mg cm^{-2}. α-MoO_3 structures were grown on Si wafer, which was placed above Mo source. The temperature of the Mo source was tuned by adding steel cooling meshes between Mo mesh and burner, and the temperature of the growth substrate was controlled by adjusting the distance between Mo mesh and Si substrate. A K-type thermocouple was used to measure the temperature of Mo mesh and substrate. α-MoO_3 with different morphologies were prepared by tuning the area density of Mo source and the temperatures of Mo source and Si substrate. A higher Mo source temperature (792 °C) facilitates Mo vapor generation, thus resulting in α-MoO_3 microplates. Lower Mo source temperatures lead to smaller nanoribbons. To demonstrate the growth of α-MoO_3 nanoribbons with a higher aspect ratio, the area density of the Mo source was halved (9 mg cm^{-2}), which reduces the partial pressure of the MoO_3 vapor. The substrate temperature was also increased. The driving force for atom attachment was thus lowered and the growth occurs preferentially along the axial [001] direction due to smaller surface energy cost. As a result, the aspect ratio was increased and α-MoO_3 nanoribbons were formed. All the α-MoO_3

samples were prepared by a 5 min deposition. Under such conditions, more than 1 cm^2 of the substrate can be uniformly covered by the flame-grown α-MoO_3 structures.

Reasons for Choosing Isotopically Pure $h^{11}BN$ and Its Growth: Three different isotopic variations were commonly used for polaritonic applications,[10,11] namely naturally abundant hBN, isotopically pure $h^{10}BN$, and isotopically pure $h^{11}BN$. As expected, heavier isotopes lead to a lower resonance frequency for the phonons. As such $h^{11}BN$ shows a lower resonance frequency compared to $h^{10}BN$. Due to this frequency shift, the hyperbolic phonon polaritons resulting from the phonon resonance of $h^{11}BN$ show a better overlap with the relevant phonon polaritons of MoO_3, which here was the main motivation for choosing $h^{11}BN$ instead of $h^{10}BN$. Compared to the naturally abundant hBN, the isotopically pure $h^{11}BN$ shows reduced losses,[10,11] which provides another advantage for polariton studies. The monoisotopic $h^{11}BN$ crystals were grown from a metal solution at atmospheric pressure as has been previously described in reference.[12]

Sample Exfoliation and Choice of Substrate: The hBN bulk samples were thinned down and transferred to ultrasmooth Au substrate using low-adhesion cleanroom tape. The ultrasmooth Au substrate was template stripped from a Si wafer (Platypus Technologies). The as-grown α-MoO_3 structures were then transferred onto hBN on gold sample using low-adhesion cleanroom tape for optical characterizations.

As Au provides a spectrally flat optical response in the infrared spectral range, using Au substrate allows a more direct interpretation of the measured spectral sample response since one does not need to consider resonant substrate excitations, for example, phonon modes. Also, bare Au substrate regions provide an ideal spectroscopic reference that here was used to normalize the measured nanospectroscopic sample response. Finally, in ultrasmooth gold, losses were reduced compared to more common evaporated Au substrates.[22]

Synchrotron-Based Infrared Nanospectroscopy: Scattering-type scanning near-field optical microscopy (s-SNOM) employs the field enhancement at the tip of an atomic force microscope to provide optical and infrared information at a wavelength-independent spatial resolution of a few 10s of nm.[50] When combined with broadband illumination and Fourier-transform infrared (FTIR) spectroscopy, s-SNOM allows one to acquire broadband infrared spectra at the nanoscale.[51] Here, SINS[34,40] was performed with a commercial s-SNOM setup (NeaSNOM by attocube) at the MET beamline of the National Synchrotron Light Source II (NSLS-II) at Brookhaven National Laboratory, Upton, USA. The synchrotron radiation was predominantly linearly polarized in the orbital plane of the electron storage ring (horizontal).[52] The optical system rotates the predominant polarization to vertical upon reaching the s-SNOM optical table and as it was incident onto the off-axis parabolic (OAP) mirror that focuses the light onto the s-SNOM tip. The OAP mirror reflects the light at a somewhat downward angle such that the light polarization includes a horizontal component as it was incident on the tip. However, the polarization remains predominantly with the E-field parallel to the tip axis. For many experimental situations, aligning the light polarization with the tip axis increases the near-field response due to the tip's increased polarizability along its axis.[53,54]

While the ultrabroadband synchrotron radiation of NSLS-II enables near-field spectroscopy in the full infrared spectral range down to <175 cm^{-1},[34] here the spectral range was limited to $\gtrsim$600 cm^{-1} by the sensitivity of the liquid-nitrogen-cooled mercury-cadmium telluride detector. As SINS measurements were performed at ambient conditions, the accessible spectral range was further limited by infrared absorption in air, explaining a lower signal-to-noise level, for example, in the spectral range $\gtrsim$1200 cm^{-1} (not shown in the manuscript). Nevertheless, the usage of accelerator-based infrared nanospectroscopy[21–23,34–37,40,44,55–57] here allows to access the bicrystal's spectral response in a much broader spectral range than usually accessible via more common table-top nanospectroscopy setups. For separation of the near-field signal from far-field background, the optical signal was demodulated at higher harmonics $n\Omega$ of the mechanical tip oscillation frequency Ω.[50,58] All near-field spectra shown in the present publication were demodulated at $n = 2$; they were normalized to reference spectra obtained on the ultrasmooth gold substrate (refer to sample fabrication).

Analytical Description of the Polariton Gap Frequency: The ray-like propagation of the polaritons allows a straightforward analytical description of the displacement δ that a polariton ray experiences when traveling through a single hyperbolic material of thickness d:[9]

$$\delta\ (\omega) = 2d\ \tan\theta\ (\omega) \tag{3}$$

where the polaritonic propagation angle $\theta(\omega)$ with respect to the surface normal is given by the ratio of the dielectric permittivities ϵ_{ip} and ϵ_{oop} along the in-plane and out-of-plane direction as $\tan\theta(\omega) = i\frac{\sqrt{\epsilon_{ip}(\omega)}}{\sqrt{\epsilon_{oop}(\omega)}}$. Note that δ as described in ref. [9] will generally be a complex quantity; in the following, interest lies in the real part of the ray displacement $\mathrm{Re}(\delta(\omega))$. For the hBN-$MoO_3$ hetero-bicrystal, the total ray displacement δ_{tot} is simply given by the sum of the ray displacement in its constituents, that is, $\delta_{tot}(\omega) = \mathrm{Re}(\delta_{hBN}(\omega)) + \mathrm{Re}(\delta_{MoO_3}(\omega))$. As shown in Figure 1f, at the gap frequency $\omega_0 = 766$ cm^{-1}, a closed polariton trajectory with no effective ray displacement was observed: $\delta_{tot}(\omega_0) = 0$. Using the equations above, this condition can also be stated as $-\frac{\mathrm{Re}(\tan(\theta_{MoO_3}(\omega_0)))}{\mathrm{Re}(\tan(\theta_{hBN}(\omega_0)))} = \frac{d_{hBN}}{d_{MoO_3}}$, that is, the gap frequency ω_0 depends on the thickness ratio $\frac{d_{hBN}}{d_{MoO_3}}$.

Analytical Dispersion of Air-MoO_3-hBN-Gold Hetero-Bicrystal: By employing source-free Maxwell equations and incorporating boundary conditions, the dispersion of the Air-MoO_3-hBN-Gold hetero-bicrystal can be expressed through a 4×4 matrix for highly confined polaritonic modes:

$$\begin{vmatrix} -e^{-qd_{MoO_3}} & e^{iq_{z1}d_{MoO_3}} & e^{-iq_{z1}d_{MoO_3}} & 0 \\ -i\epsilon_1 q e^{-qd_{MoO_3}} & \epsilon_{M,oop}q_{z1}e^{iq_{z1}d_{MoO_3}} & -\epsilon_{M,oop}q_{z1}e^{-iq_{z1}d_{MoO_3}} & 0 \\ 0 & 1 & 1 & 2i\sin(q_{z2}d_{hBN}) \\ 0 & \epsilon_{M,oop}q_{z1} & -\epsilon_{M,oop}q_{z1} & 2\epsilon_{h,oop}q_{z2}\cos(q_{z2}d_{hBN}) \end{vmatrix} = 0 \tag{4}$$

Here, ϵ_1, $\epsilon_{M,i}$, and $\epsilon_{h,i}$ ($i \in$ ip, oop) represent the background permittivity, MoO_3 permittivity, and hBN permittivity, respectively. The in-plane wavevector q, along with $q_{z1} = \frac{q}{\psi_{MoO_3}}$, $q_{z2} = \frac{q}{\psi_{hBN}}$, $\psi_{MoO_3} = \sqrt{-\frac{\epsilon_{M,oop}}{\epsilon_{M,\ ip}}}$, and $\psi_{hBN} = \sqrt{-\frac{\epsilon_{h,oop}}{\epsilon_{h,\ ip}}}$, contribute to the intricate structure of the equation. After the straightforward simplification, this equation can be simplified as follows:[26]

$$q = \frac{\psi_{MoO_3}}{d_{MoO_3}}\left[\mathrm{atan}\left(-\frac{\epsilon_{M,oop}}{\psi_{MoO_3}}\frac{1}{\epsilon_1}\right) + \mathrm{atan}\left(-\frac{\epsilon_{M,oop}}{\psi_{MoO_3}}\frac{\psi_{hBN}\tan\left(\frac{qd_{hBN}}{\psi_{hBN}}\right)}{\epsilon_{h,oop}}\right) + l\pi\right],\ l = 0, 1, 2\ldots \tag{5}$$

In the dispersion calculation from this equation, considering the dispersion of materials, it was imperative to sweep through frequencies (in real numbers), and l in the specified range to solve for q. Introducing the consideration of material loss transforms q into a complex number, leading to the definition of the quality factor $Q(\omega) = \frac{\mathrm{Re}(q)}{\mathrm{Im}(q)}$. It is important to note that in the calculation process, q is a complex number obtained by sweeping each ω. In regions where the band was nearly flat, the authors were constrained to derive only a single solution from the analytical equations, despite the existence of multiple q values corresponding to ω. This limitation results in the absence of Q factors in certain regions of Figure 4. For the calculation of the gap width, it was crucial to identify the gap range near the intersection point of single MoO_3 polariton modes and single hBN polariton modes (depicted in Figure 1c,d). Additionally, the intersection points of the single MoO_3 polariton mode and the hetero-bicrystals polariton mode were key parameters. The initial step involves solving for the first intersection point between the upper band (above the gap) of hetero-bicrystals and the band of single MoO_3, denoted as (q_0, ω_u). Subsequently, by fixing $q = q_0$, the frequency ω_d of the lower band of hetero-bicrystals (below the gap) was determined. The gap width

$\Delta\omega = \omega_u - \omega_d$ was then defined. In specific regions, precise determination of ω_d was challenging due to its proximity to the resonance frequency of hBN at $\omega_{TO,oop}^{hBN} = 755\ cm^{-1}$. To elucidate this phenomenon, the thickness of the MoO_3 slab was maintained at 100 nm while altering the thickness of the continuous hBN layer. The resulting variations in ω_d, ω_c, and ω_u are illustrated in Figure S1, Supporting Information. Figure S2, Supporting Information illustrates the impact of different MoO_3 thicknesses, with all samples supporting the assertions in the main text.

Numerical Simulations: The simulation results were obtained using a well-established full-wave simulation method demonstrated in multiple previous publications.[16,59] In the simulations, the illuminated s-SNOM tip was modeled as a vertically oriented point dipole source located 200 nm above the top surface of the MoO_3 microcrystal. The cross-sectional electric field distributions shown in Figure 1f,g as well as Figures S3 and S4, Supporting Information were obtained from 2D FDTD simulations on a stack of MoO_3/hBN/gold. The in-plane dimensions of the layers were assumed to be infinitely large and their thicknesses were varied.

3D FDTD simulations were used to simulate the hyperspectral images and the electric field distributions in Figure 5. The dimensions of the MoO_3 microcrystal were precisely based on the AFM measurement. To approximate the scattering s-SNOM signal from the tip, the z-component of the electric field 150 nm below the dipole was considered. The simulations of the hyperspectral images were rather computationally demanding since the dipole needs to emit broadband light and the position of the dipole needs to be changed in a fine resolution (20 nm) to mimic the tip scanning in the experiment, resulting in a large number (71 for Figure 5b and 36 for Figure 5c) of FDTD runs. The fast FDTD solver Tidy3D was used, where the simulations were hardware-accelerated and parallelized to significantly reduce the solving time.

Supporting Information

Supporting Information is available from the Wiley Online Library or from the author.

Acknowledgements

J.A.F. acknowledges the National Science Foundation under award nos. 2103721 and 1804224 and the Air Force Office of Scientific Research under award no. FA9550-18-1-0070. R.A.M. acknowledges the São Paulo Research Foundation under award no. 2022/06709 0, the Brazilian Synchrotron Light Laboratory (LNLS), and the State University of Campinas (UNICAMP). J.H.E. acknowledges the Office of Naval Research under award no. N00014-20-1-2474 for h11BN crystal growth. M.L. acknowledges ICAM and the Gordon and Betty Moore Foundation under award no. GBMF9616 for a QuantEmX travel grant, and the Gordon and Betty Moore Foundation under award no. DOI: 10.37807/gbmf12258 for supporting the development of novel polaritonic materials. D.N.B. and M.L. acknowledge the Programmable Quantum Materials (Pro-QM) Energy Frontier Research Center (EFRC), which was funded by the U.S. Department of Energy (DOE), Office of Science, Basic Energy Sciences (BES), under award no. DE-SC0019443. H.Y. and T.F.H. acknowledge support from the Office of Naval Research through the MURI on Twist Optics under award no. N00014-23-1-2567 and the Gordon and Betty Moore Foundation's EPiQS Initiative through grant GBMF9462 for analysis and simulations. J.H. acknowledges support from NTT Research for a graduate fellowship. G.H. acknowledges the Nanyang Assistant Professorship Start-up Grant, Ministry of Education (Singapore) under AcRF TIER1 (RG61/23), and the National Research Foundation of Singapore under award no. CRP22-2019-0064. Near-field instrument construction at BNL was supported by the U.S. Department of Energy, Office of Science, National Quantum Information Science Research Centers, Co-design Center for Quantum Advantage (C2QA) under award no. DE-SC0012704. Synchrotron-based infrared nanospectroscopy was performed at the MET beamline of the National Synchrotron Light Source II, a U.S. Department of Energy (DOE) Office of Science User Facility operated for the DOE Office of Science by Brookhaven National Laboratory under award no. DE-SC0012704.

Conflict of Interest

X.C. is currently affiliated with Flexcompute Inc., which is the developer of the Tidy3D simulation software used in this study. This affiliation has not influenced the study design, data collection and analysis, decision to publish, or preparation of the manuscript. All other authors declare no competing interests.

Author Contributions

L.W. and S.-J.Y. contributed equally to this work. L.W., S.-J.Y., G.L.C., M.L., and J.A.F. conceived the study. S.-J.Y. and J.A.F. designed the samples. S.-J.Y., H.Y., Y.J., J.H., and X.Z. grew the MoO_3 and fabricated the samples. E.J. and J.H.E. grew the hBN crystals. L.W. and S.-J.Y. performed the experimental measurements with support from T.F.H., C.C.H., G.L.C., M.L., and J.A.F. L.W., S.-J.Y., and R.A.M. analyzed the experimental data with input from H.Y., G.L.C., and M.L. X.C. performed the numerical simulations. L.W., S.-J.Y., X.C., R.A.M., L.X., and J.H. derived the analytical description and performed the analytical calculations. D.N.B. helped to support the nanoFTIR facility at BNL. L.W., S.-J.Y., M.L., and J.A.F. drafted the manuscript with input from all other authors.

Data Availability Statement

The data that support the findings of this study are available from the corresponding author upon reasonable request.

Keywords

metamaterials, nanophotonics, phonon polaritons, synchrotron infrared nanospectroscopy, van der Waals materials

Received: January 25, 2024
Revised: April 5, 2024
Published online: June 21, 2024

[1] Q. Zhang, G. Hu, W. Ma, P. Li, A. Krasnok, R. Hillenbrand, A. Alù, C.-W. Qiu, *Nature* **2021**, *597*, 187.
[2] D. N. Basov, M. M. Fogler, F. J. Garcia de Abajo, *Science* **2016**, *354*, aag1992.
[3] D. N. Basov, A. Asenjo-Garcia, P. J. Schuck, X. Zhu, A. Rubio, *Nanophotonics* **2020**, *10*, 549.
[4] J. D. Caldwell, A. V. Kretinin, Y. Chen, V. Giannini, M. M. Fogler, Y. Francescato, C. T. Ellis, J. G. Tischler, C. R. Woods, A. J. Giles, M. Hong, K. Watanabe, T. Taniguchi, S. A. Maier, K. S. Novoselov, *Nat. Commun.* **2014**, *5*, 5221.
[5] S. Dai, Z. Fei, Q. Ma, A. S. Rodin, M. Wagner, A. S. McLeod, M. K. Liu, W. Gannett, W. Regan, K. Watanabe, T. Taniguchi, M. Thiemens, G. Dominguez, A. H. C. Neto, A. Zettl, F. Keilmann, P. Jarillo-Herrero, M. M. Fogler, D. N. Basov, *Science* **2014**, *343*, 1125.
[6] S. Dai, Q. Ma, M. K. Liu, T. Andersen, Z. Fei, M. D. Goldflam, M. Wagner, K. Watanabe, T. Taniguchi, M. Thiemens, F. Keilmann, G. C. a. M. Janssen, S.-E. Zhu, P. Jarillo-Herrero, M. M. Fogler, D. N. Basov, *Nat. Nanotechnol.* **2015**, *10*, 682.
[7] P. Li, M. Lewin, A. V. Kretinin, J. D. Caldwell, K. S. Novoselov, T. Taniguchi, K. Watanabe, F. Gaussmann, T. Taubner, *Nat. Commun.* **2015**, *6*, 7507.
[8] Z. Shi, H. A. Bechtel, S. Berweger, Y. Sun, B. Zeng, C. Jin, H. Chang, M. C. Martin, M. B. Raschke, F. Wang, *ACS Photonics* **2015**, *2*, 790.

[9] S. Dai, Q. Ma, T. Andersen, A. S. Mcleod, Z. Fei, M. K. Liu, M. Wagner, K. Watanabe, T. Taniguchi, M. Thiemens, F. Keilmann, P. Jarillo-Herrero, M. M. Fogler, D. N. Basov, *Nat. Commun.* **2015**, *6*, 6963.
[10] M. Chen, Y. Zhong, E. Harris, J. Li, Z. Zheng, H. Chen, J.-S. Wu, P. Jarillo-Herrero, Q. Ma, J. H. Edgar, X. Lin, S. Dai, *Nat. Commun.* **2023**, *14*, 4782.
[11] A. J. Giles, S. Dai, I. Vurgaftman, T. Hoffman, S. Liu, L. Lindsay, C. T. Ellis, N. Assefa, I. Chatzakis, T. L. Reinecke, J. G. Tischler, M. M. Fogler, J. H. Edgar, D. N. Basov, J. D. Caldwell, *Nat. Mater.* **2018**, *17*, 134.
[12] S. Liu, R. He, L. Xue, J. Li, B. Liu, J. H. Edgar, *Chem. Mater.* **2018**, *30*, 6222.
[13] S. Dai, J. Quan, G. Hu, C.-W. Qiu, T. H. Tao, X. Li, A. Alù, *Nano Lett.* **2019**, *19*, 1009.
[14] G. Hu, J. Shen, C.-W. Qiu, A. Alù, S. Dai, *Adv. Opt. Mater.* **2020**, *8*, 1901393.
[15] A. J. Sternbach, S. L. Moore, A. Rikhter, S. Zhang, R. Jing, Y. Shao, B. S. Y. Kim, S. Xu, S. Liu, J. H. Edgar, A. Rubio, C. Dean, J. Hone, M. M. Fogler, D. N. Basov, *Science* **2023**, *379*, 555.
[16] W. Ma, P. Alonso-González, S. Li, A. Y. Nikitin, J. Yuan, J. Martín-Sánchez, J. Taboada-Gutiérrez, I. Amenabar, P. Li, S. Vélez, C. Tollan, Z. Dai, Y. Zhang, S. Sriram, K. Kalantar-Zadeh, S.-T. Lee, R. Hillenbrand, Q. Bao, *Nature* **2018**, *562*, 557.
[17] G. Hu, Q. Ou, G. Si, Y. Wu, J. Wu, Z. Dai, A. Krasnok, Y. Mazor, Q. Zhang, Q. Bao, C.-W. Qiu, A. Alù, *Nature* **2020**, *582*, 209.
[18] M. Chen, X. Lin, T. H. Dinh, Z. Zheng, J. Shen, Q. Ma, H. Chen, P. Jarillo-Herrero, S. Dai, *Nat. Mater.* **2020**, *19*, 1307.
[19] Z. Dai, G. Hu, G. Si, Q. Ou, Q. Zhang, S. Balendhran, F. Rahman, B. Y. Zhang, J. Z. Ou, G. Li, A. Alù, C.-W. Qiu, Q. Bao, *Nat. Commun.* **2020**, *11*, 6086.
[20] T. V. A. G. Oliveira, T. Nörenberg, G. Álvarez-Pérez, L. Wehmeier, J. Taboada-Gutiérrez, M. Obst, F. Hempel, E. J. H. Lee, J. M. Klopf, I. Errea, A. Y. Nikitin, S. C. Kehr, P. Alonso-González, L. M. Eng, *Adv. Mater.* **2021**, *33*, 2005777.
[21] I. D. Barcelos, T. A. Canassa, R. A. Mayer, F. H. Feres, E. G. de Oliveira, A.-M. B. Goncalves, H. A. Bechtel, R. O. Freitas, F. C. B. Maia, D. C. B. Alves, *ACS Photonics* **2021**, *8*, 3017.
[22] S.-J. Yu, Y. Jiang, J. A. Roberts, M. A. Huber, H. Yao, X. Shi, H. A. Bechtel, S. N. Gilbert Corder, T. F. Heinz, X. Zheng, J. A. Fan, *ACS Nano* **2022**, *16*, 3027.
[23] Y. Zeng, T. Sun, R. Chen, W. Ma, Q. Yan, D. Lu, T. Qin, C. Hu, X. Yang, P. Li, *Opt. Express* **2023**, *31*, 28010.
[24] H. Hu, N. Chen, H. Teng, R. Yu, M. Xue, K. Chen, Y. Xiao, Y. Qu, D. Hu, J. Chen, Z. Sun, P. Li, F. J. G. de Abajo, Q. Dai, *Science* **2023**, *379*, 558.
[25] M. He, L. Hoogendoorn, S. Dixit, Z. Pan, G. Lu, K. Diaz-Granados, D. Li, J. D. Caldwell, *Nano Lett.* **2023**, *23*, 5035.
[26] S.-J. Yu, H. Yao, G. Hu, Y. Jiang, X. Zheng, S. Fan, T. F. Heinz, J. A. Fan, *ACS Nano* **2023**, *17*, 23057.
[27] D. N. Basov, R. D. Averitt, D. Hsieh, *Nat. Mater.* **2017**, *16*, 1077.
[28] C. R. Woods, P. Ares, H. Nevison-Andrews, M. J. Holwill, R. Fabregas, F. Guinea, A. K. Geim, K. S. Novoselov, N. R. Walet, L. Fumagalli, *Nat. Commun.* **2021**, *12*, 347.
[29] Z. Zheng, Q. Ma, Z. Bi, S. de la Barrera, M.-H. Liu, N. Mao, Y. Zhang, N. Kiper, K. Watanabe, T. Taniguchi, J. Kong, W. A. Tisdale, R. Ashoori, N. Gedik, L. Fu, S.-Y. Xu, P. Jarillo-Herrero, *Nature* **2020**, *588*, 71.
[30] Z. Fei, G. O. Andreev, W. Bao, L. M. Zhang, A. S. McLeod, C. Wang, M. K. Stewart, Z. Zhao, G. Dominguez, M. Thiemens, M. M. Fogler, M. J. Tauber, A. H. Castro-Neto, C. N. Lau, F. Keilmann, D. N. Basov, *Nano Lett.* **2011**, *11*, 4701.
[31] J. Chen, M. Badioli, P. Alonso-González, S. Thongrattanasiri, F. Huth, J. Osmond, M. Spasenović, A. Centeno, A. Pesquera, P. Godignon, A. Z. Elorza, N. Camara, F. J. G. de Abajo, R. Hillenbrand, F. H. L. Koppens, *Nature* **2012**, *487*, 77.
[32] Z. Fei, A. S. Rodin, G. O. Andreev, W. Bao, A. S. McLeod, M. Wagner, L. M. Zhang, Z. Zhao, M. Thiemens, G. Dominguez, M. M. Fogler, A. H. C. Neto, C. N. Lau, F. Keilmann, D. N. Basov, *Nature* **2012**, *487*, 82.
[33] T. Nörenberg, G. Álvarez-Pérez, M. Obst, L. Wehmeier, F. Hempel, J. M. Klopf, A. Y. Nikitin, S. C. Kehr, L. M. Eng, P. Alonso-González, T. V. A. G. de Oliveira, *ACS Nano* **2022**, *16*, 20174.
[34] L. Wehmeier, M. Liu, S. Park, H. Jang, D. N. Basov, C. C. Homes, G. L. Carr, *ACS Photonics* **2023**, *10*, 4329.
[35] I. D. Barcelos, H. A. Bechtel, C. J. S. de Matos, D. A. Bahamon, B. Kaestner, F. C. B. Maia, R. O. Freitas, *Adv. Opt. Mater.* **2020**, *8*, 1901091.
[36] F. H. Feres, R. A. Mayer, L. Wehmeier, F. C. B. Maia, E. R. Viana, A. Malachias, H. A. Bechtel, J. M. Klopf, L. M. Eng, S. C. Kehr, J. C. González, R. O. Freitas, I. D. Barcelos, *Nat. Commun.* **2021**, *12*, 1995.
[37] O. Khatib, H. A. Bechtel, M. C. Martin, M. B. Raschke, G. L. Carr, *ACS Photonics* **2018**, *5*, 2773.
[38] F. J. Alfaro-Mozaz, P. Alonso-González, S. Vélez, I. Dolado, M. Autore, S. Mastel, F. Casanova, L. E. Hueso, P. Li, A. Y. Nikitin, R. Hillenbrand, *Nat. Commun.* **2017**, *8*, 15624.
[39] I.-H. Lee, M. He, X. Zhang, Y. Luo, S. Liu, J. H. Edgar, K. Wang, P. Avouris, T. Low, J. D. Caldwell, S.-H. Oh, *Nat. Commun.* **2020**, *11*, 3649.
[40] H. A. Bechtel, E. A. Muller, R. L. Olmon, M. C. Martin, M. B. Raschke, *Proc. Natl. Acad. Sci. U. S. A.* **2014**, *111*, 7191.
[41] J. B. Pendry, *Phys. Rev. Lett.* **2000**, *85*, 3966.
[42] N. Fang, H. Lee, C. Sun, X. Zhang, *Science* **2005**, *308*, 534.
[43] T. Taubner, D. Korobkin, Y. Urzhumov, G. Shvets, R. Hillenbrand, *Science* **2006**, *313*, 1595.
[44] S. C. Kehr, Y. M. Liu, L. W. Martin, P. Yu, M. Gajek, S.-Y. Yang, C.-H. Yang, M. T. Wenzel, R. Jacob, H.-G. von Ribbeck, M. Helm, X. Zhang, L. M. Eng, R. Ramesh, *Nat. Commun.* **2011**, *2*, 249.
[45] M. Fehrenbacher, S. Winnerl, H. Schneider, J. Döring, S. C. Kehr, L. M. Eng, Y. Huo, O. G. Schmidt, K. Yao, Y. Liu, M. Helm, *Nano Lett.* **2015**, *15*, 1057.
[46] J. A. Roberts, S.-J. Yu, P.-H. Ho, S. Schoeche, A. L. Falk, J. A. Fan, *Nano Lett.* **2019**, *19*, 3131.
[47] J. A. Roberts, P.-H. Ho, S.-J. Yu, X. Wu, Y. Luo, W. L. Wilson, A. L. Falk, J. A. Fan, *Phys. Rev. Appl.* **2020**, *14*, 044006.
[48] A. Fali, S. T. White, T. G. Folland, M. He, N. A. Aghamiri, S. Liu, J. H. Edgar, J. D. Caldwell, R. F. Haglund, Y. Abate, *Nano Lett.* **2019**, *19*, 7725.
[49] A. Opala, M. Furman, M. Król, R. Mirek, K. Tyszka, B. Seredyński, W. Pacuski, J. Szczytko, M. Matuszewski, B. Piętka, *Optica* **2023**, *10*, 1111.
[50] X. Chen, D. Hu, R. Mescall, G. You, D. N. Basov, Q. Dai, M. Liu, *Adv. Mater.* **2019**, *31*, 1804774.
[51] S. Amarie, T. Ganz, F. Keilmann, *Opt. Express* **2009**, *17*, 21794.
[52] P. Dumas, M. C. Martin, G. L. Carr, in *Synchrotron Light Sources and Free-Electron Lasers* (Eds: E. J. Jaeschke, S. Khan, J. R. Schneider, J. B. Hastings), Springer International Publishing, Cham **2020**, pp. 2059–2113.
[53] A. Cvitkovic, N. Ocelic, R. Hillenbrand, *Opt. Express* **2007**, *15*, 8550.
[54] A. S. McLeod, P. Kelly, M. D. Goldflam, Z. Gainsforth, A. J. Westphal, G. Dominguez, M. H. Thiemens, M. M. Fogler, D. N. Basov, *Phys. Rev. B* **2014**, *90*, 085136.
[55] L. Wehmeier, T. Nörenberg, T. V. A. G. de Oliveira, J. M. Klopf, S.-Y. Yang, L. W. Martin, R. Ramesh, L. M. Eng, S. C. Kehr, *Appl. Phys. Lett.* **2020**, *116*, 071103.

[56] J. Barnett, L. Wehmeier, A. Heßler, M. Lewin, J. Pries, M. Wuttig, J. M. Klopf, S. C. Kehr, L. M. Eng, T. Taubner, *Nano Lett.* **2021**, *21*, 9012.
[57] L. Wehmeier, D. Lang, Y. Liu, X. Zhang, S. Winnerl, L. M. Eng, S. C. Kehr, *Phys. Rev. B* **2019**, *100*, 035444.
[58] B. Knoll, F. Keilmann, *Opt. Commun.* **2000**, *182*, 321.
[59] G. Álvarez-Pérez, T. G. Folland, I. Errea, J. Taboada-Gutiérrez, J. Duan, J. Martín-Sánchez, A. I. F. Tresguerres-Mata, J. R. Matson, A. Bylinkin, M. He, W. Ma, Q. Bao, J. I. Martín, J. D. Caldwell, A. Y. Nikitin, P. Alonso-González, *Adv. Mater.* **2020**, *32*, 1908176.